

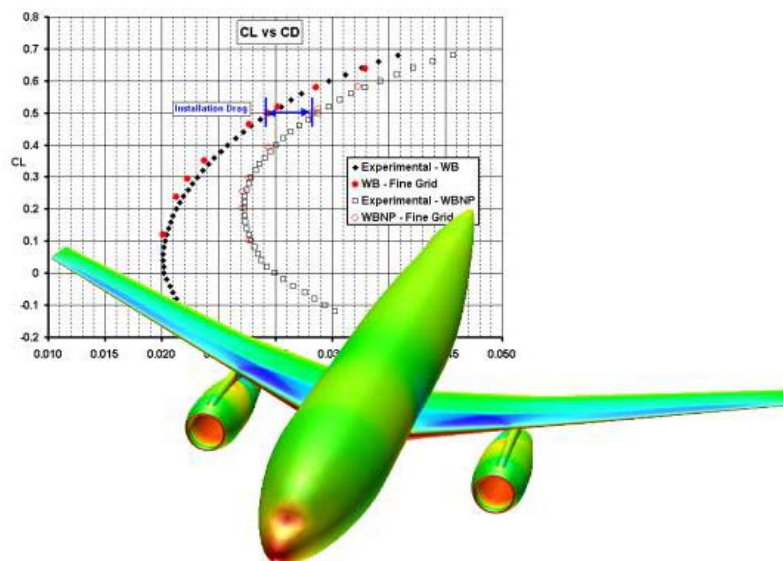


AIAA 2004-0395

## Accurate Drag Prediction Using Cobalt

Kenneth E. Wurtzler  
Cobalt Solutions, LLC

Scott A. Morton  
United States Air Force Academy



**42<sup>nd</sup> Aerospace Sciences Meeting & Exhibit**  
**5-8 January, 2004**  
**Reno, Nevada**

# Accurate Drag Prediction Using Cobalt

**Kenneth E. Wurtzler**

Cobalt Solutions, LLC  
Dayton, OH

**Scott A. Morton**

Department of Aeronautics  
United States Air Force Academy  
USAF Academy, CO 80840

## Abstract

The technical objective of the 2<sup>nd</sup> AIAA CFD Drag Prediction Workshop is to assess the state-of-the-art computational methods as practical aerodynamic tools for aircraft force and moment prediction of increasingly complex geometries. With more emphasis being placed on CFD methods to evaluate aircraft designs early in the design process, the ability to accurately predict the forces and moments, specifically drag, on an airliner configuration is important. Using the CFD code Cobalt, force and moment calculations are obtained on a civil transport geometry with and without engine nacelle and pylon. Comparisons with experimental data show consistent agreement with forces and moments, wing Cp data, and qualitative data. Installation drag for the nacelle/pylon is well predicted. Relevance of the importance of the grid and robustness of the flow solver to the overall accuracy of the results is discussed.

## Nomenclature

<i>alpha</i>	angle of attack
<i>c</i>	Wing root chord, 14.1 cm
<i>M</i>	Mach number, 0.75
<i>Re</i>	Reynolds number, $U_\infty c/v_\infty$
<i>COARSE</i>	original coarse grid
<i>MEDIUM</i>	original medium grid
<i>FINE</i>	original fine grid
<i>WBA</i>	Wing-Body adapted grid
<i>WBNPA</i>	Wing-Body-Nacelle-Pylon adapted grid

## Introduction

Government and university labs and the aircraft industry have been developing computational methods suitable for aircraft loads prediction for decades. Only recently have computer codes been available that can provide accuracy and robustness for general geometries at flight Reynolds numbers.

In an effort to document the degree to which current CFD codes can predict the loads of a generic configuration, the AIAA sponsored the 2<sup>nd</sup> CFD Drag Prediction Workshop in June of 2003. The technical objective was to assess the state-of-the-art computational methods as practical aerodynamic tools for aircraft force and moment prediction of increasingly complex geometries and to build on the results of the 1st Drag Prediction Workshop by investigating incremental drag as well as total drag. Special emphasis was placed on drag prediction accuracy and component drag increments. A secondary objective was to identify areas needing additional research and development.

In order to meet these objectives, the workshop provided a common geometry and reliable, available test data for comparison. The complete workshop case list included a single-point grid convergence study, drag polar, fully turbulent versus tripped boundary layer, and drag rise computations.

In order for CFD tools to be useful, they must act as a predictive method with little reliance on previous design data. Aircraft designs that progress with little geometric difference provide an easy method to ‘calibrate’ CFD codes. Results are adjusted according to the error from the previous design result. The force and moment data that this calibration process provides may not be consistent with the flow physics. Therefore, this process is unreliable in the face of unsteady flow phenomena such as shock/boundary layer interaction and separation. It also cannot be used for radical new designs and flight regimes that have no database of force and moment data associated with it.

It is also important to maintain the geometric integrity so as to provide for a precise comparison with the wind tunnel results. Modifying the geometry according to previous computational results removes the predictive capability of CFD for

new designs. Any modification also introduces unknown error into the solution.

Accurate force and moment prediction must also be consistent across all forces and moments. This will ensure the correct pressure distribution for the lift is obtained around the aircraft. It will also enable better prediction of installation drag along with prediction of the absolute force values. The current work seeks to demonstrate the ability of the computer code *Cobalt* to provide these accurate simulations of a generic airliner configuration.

### Computational Method

*Cobalt* is a commercial hybrid Navier-Stokes flow solver. *Cobalt* is highly robust and accurate and possesses great parallel performance. *Cobalt* solves the Navier-Stokes equations, including an improved spatial operator and improved temporal integration. The code has been validated on a number of problems.<sup>1</sup> Tomaro, et al., converted *Cobalt* from explicit to implicit, enabling CFL numbers as high as one million.<sup>2</sup> Grismer, et al., then parallelized the code, yielding a linear speedup on as many as 1024 processors.<sup>3</sup> Forsythe, et al., provided a comprehensive testing and validation of the RANS models, including the Spalart-Allmaras, Wilcox  $k-\omega$ , and Menter's SST turbulence models.<sup>4</sup>

The numerical method is a cell-centered finite volume approach applicable to arbitrary cell topologies, for example, hexahedra, prisms, tetrahedra. The spatial operator uses the exact Riemann solver of Gottlieb and Groth<sup>5</sup>, least-squares gradient calculations using QR factorization to provide second-order accuracy in space, and total variation diminishing flux limiters to limit extremes at cell faces. A point implicit method using analytic first-order inviscid and viscous Jacobians is used for advancement of the discretized system. For time-accurate computations, a Newton subiteration scheme is employed, and the method is second-order accurate in time.

### Grids

The computational grids were created using the software programs *Gridtool*<sup>6</sup>, to develop the surface point distributions and background sources, and *VGRIDns*<sup>7</sup> to create the volume grid. The outer dimensions of the computational domain were  $-850\text{cm} < X < 850\text{cm}$  (streamwise),  $0\text{cm} < Y < 700\text{cm}$  (spanwise),  $-450\text{cm} < Z < 450\text{cm}$  (surface normal), where the wing root chord is 14.1cm. A half-span assumption was made for all grids generated. Initially, for the wing-body and wing-body-nacelle-

pylon configurations, three grids were constructed to complete a grid resolution study (COARSE, MEDIUM, and FINE).

The initial grids for the wing/body and wing/body/nacelle/pylon configurations were created with surface triangles concentrated on the leading edge and trailing edge. Surface triangles on the upper and lower wing surface were stretched by a factor of 1.5. The trailing edge had a thickness to it and much attention was paid to placing the proper number of cells across the edge.

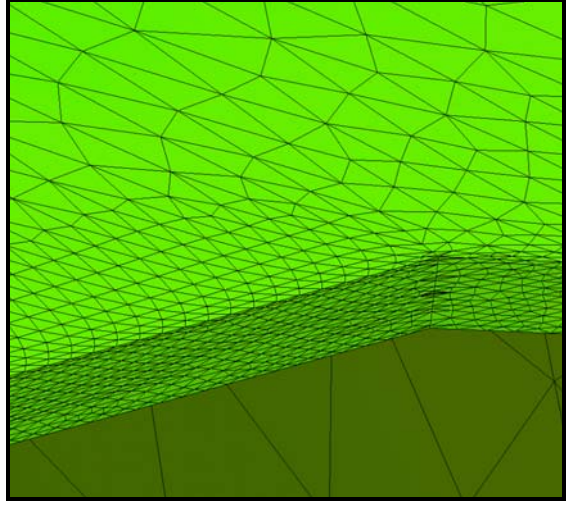


Figure 1: Fine grid wing/trailing edge surface mesh.

The fine grid had approximately 30 cells across the trailing edge with the medium and coarse grids having less (see Figure 2).

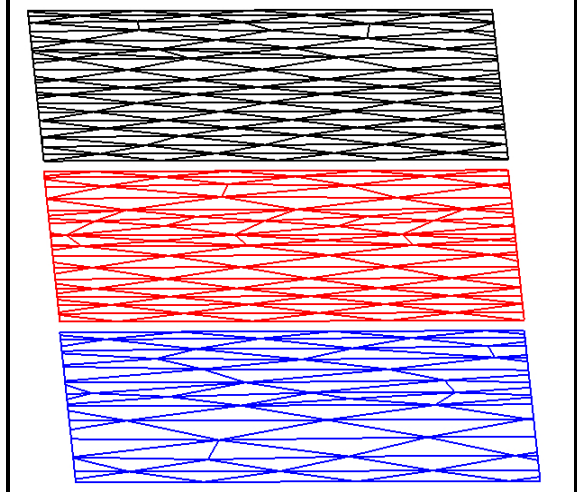


Figure 2: Trailing edge surface grid of the FINE (top), MEDIUM (middle), and COARSE (bottom) grids.

Since the trailing edge area is of very high aspect ratio, the cells on that particular surface were stretched and also had a high aspect ratio. This was necessary to avoid an impossibly high number of cells if no stretching was used. The stretching factor for the trailing edge cells for the fine grid was on the order of four. It was also difficult to maintain a smooth distribution of cells across the trailing edge. The distribution of surface triangles for the wing/body grids is shown in Table 1 and the wing/body/nacelle/pylon grids is shown in Table 2. The emphasis of cells on the trailing edge is obvious from Tables 1 and 2, with the smallest area of the listed components (the trailing edge) having the first or second largest number of triangles on its surface.

	Fine Grid	Medium Grid	Coarse Grid
Upper Wing	63,075	48,839	38,660
Lower Wing	61,499	46,284	38,625
Trailing Edge	62,437	48,138	38,963
Wing Tip	2,531	1,891	1,516
Fuselage	10,591	8,082	6,377

**Table 1: Distribution of surface triangles for wing/body geometry.**

	Fine Grid	Medium Grid	Coarse Grid
Upper Wing	63,075	48,839	38,660
Lower Wing	61,499	46,284	38,625
Trailing Edge	62,437	48,138	38,963
Wing Tip	2,531	1,891	1,516
Fuselage	10,591	8,082	6,377
Nacelle	40,351	30,589	24,237
Pylon	9,036	6,889	5,438

**Table 2: Distribution of surface triangles for wing/body/nacelle/pylon geometry.**

The grids for the grid resolution study were generated by changing the *ifact* value in *VGRIDns*. This value globally scaled the distribution of points on the surface and in the volume grid creating a set of grids consistently more refined in all three coordinate directions. The final grid output from *VGRIDns* was comprised solely of tetrahedral cells. The grid utility *Blacksmith* was used to combine tets in the boundary layer into prisms. Each layer created only contained prisms – there were no mix of prisms and tets in a layer. This process reduced the overall numbers of cells and also created higher quality cells in the boundary layer. The value of *ifact*, number of surface triangles, and resultant grid size for the wing/body and the

wing/body/nacelle/pylon geometry are shown in Tables 3 and 4, respectively.

<b>Coarse Grid</b>	<b>ifact = 1.30</b>	122,141 surface triangles 5,268,540 tets 3,802,848 tets/prisms
<b>Medium Grid</b>	<b>ifact = 1.15</b>	153,234 surface triangles 6,714,822 tets 4,876,014 tets/prisms
<b>Fine Grid</b>	<b>ifact = 1.0</b>	200,133 surface triangles 8,975,988 tets 6,574,392 tets/prisms

**Table 3 Wing/body grids with surface triangles and grid size.**

<b>Coarse Grid</b>	<b>ifact = 1.30</b>	139,600 surface triangles 6,114,050 tets 4,718,050 tets/prisms
<b>Medium Grid</b>	<b>ifact = 1.15</b>	175,550 surface triangles 7,797,527 tets 6,042,027 tets/prisms
<b>Fine Grid</b>	<b>ifact = 1.0</b>	232,572 surface triangles 10,528,768 tets 8,202,958 tets/prisms

**Table 4: Wing/body/nacelle/pylon grids with surface triangles and grid size.**

Adaptive mesh refinement (AMR) was performed using a version of *VGRIDns*. Pirzadeh<sup>8</sup> presented a method based on a tetrahedral unstructured grid technology developed at NASA Langley Research Center with application to two configurations with vortex dominated flowfields. The mesh refinement only occurred outside of the boundary layer and the fine grid was chosen as the start for both WB and WBNP geometry since it had the highest quality surface grid. A flow solution was computed for the fine grid described above, and the solution was used to create an AMR grid by eliminating all cells within an isosurface of vorticity at a particular level. The tetrahedral grid was then grown inside of the iso-surface with an *ifact* of 0.6.

A comparison of the original grid and the AMR grid for the WB geometry is shown in Figure 3 and for the WBNP geometry in Figure 4. The red region is the adapted region inside of the iso-surface. Outside of the adapted region, the grids are equivalent. The

adapted WB grid has 8,083,504 cells and the adapted WBNP grid has 8,872,611 cells.

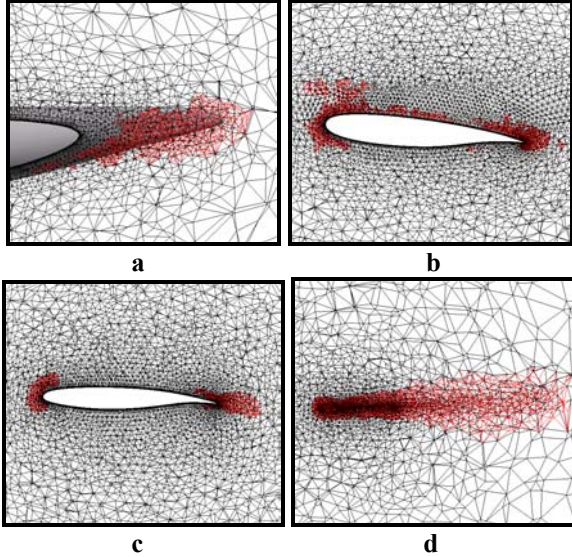


**Figure 3: Comparison of grid density at span stations (a) 0.5, (b) 0.8, (c) 2.2 (d) wing tip.**

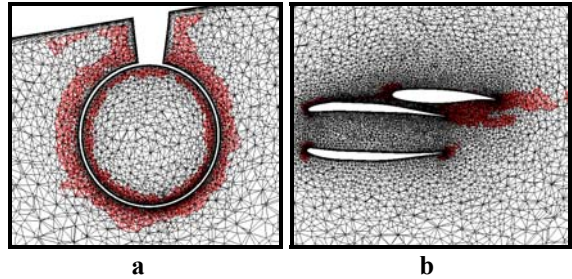


**Figure 4: Comparison of grid density (a) aft of nacelle and (b) inboard of pylon.**

All of the grids in this study consist of an inner region of approximately 8 layers of prisms for the boundary layer, with a wall normal spacing in viscous wall units less than 1, and an outer region of tetrahedra. The prism dimensions on the surface were a factor of approximately 200 times larger than the wall normal dimension for all grids.

## Results

The single-point convergence study and the drag polar portion of the drag prediction workshop are presented and discussed for the WB and WBNP geometries. WB solutions were run for 500 iterations and the WBNP solutions were run for 1000 iterations, starting from freestream conditions. Typical Convergence data for the wing-body fine grid is shown in Figure 5. Menter's SST turbulence model was used for all calculations.

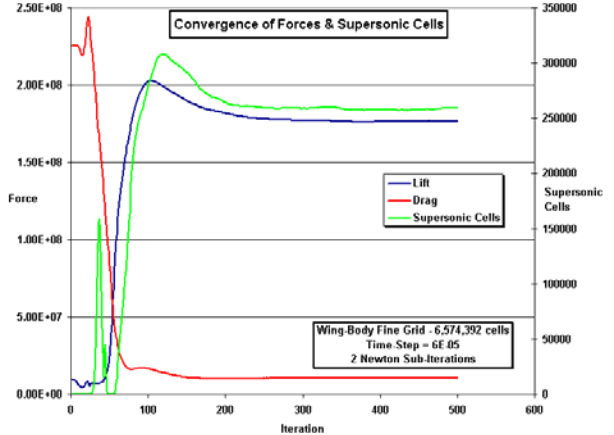


**Figure 5: Convergence for the wing-body fine grid at alpha = 0.49°.**

Initially, solutions were computed for various grids at a 0.49° angle of attack consistent with the angle of attack the experiment reported  $C_L=0.5$ . Next, solutions for an angle of attack of 0° were computed and interpolation was used to determine the computed angle of attack corresponding to  $C_L=0.5$ . A solution was run at this angle of attack to verify the value of  $C_L$ . Finally, a range of angles of attack were computed and the  $C_L$ ,  $C_D$ , and  $C_M$  values reported for the WB and WBNP configurations. All of the solutions in the single point and drag polar studies were for  $M = 0.75$ ,  $Re = 3 \times 10^6$ , and a fully turbulent assumption. Comparisons were made with wind tunnel force and moment data and pressure data.

The WB single-point comparison data for the fine and adapted grids at alpha = 0.49° is presented in Table 5. The experimental alpha for CL = 0.50 is 0.49° and the computationally predicted alpha is 0.31°.

	Experimental	Cobalt	% Diff
$C_L$	<b>0.4984</b>	Fine <b>0.5190</b> Ad <b>0.5142</b>	<b>3.9%</b> <b>3.2%</b>
$C_D$	<b>0.0294</b>	Fine <b>0.0302</b> Ad <b>0.0301</b>	<b>2.6%</b> <b>2.3%</b>
$C_M$	<b>-0.1213</b>	Fine <b>-0.1185</b> Ad <b>-0.1170</b>	<b>2.4%</b> <b>3.5%</b>

**Table 5: Single-point data for the fine and adapted grids at alpha=0.49° for the wing- body case.**

Figures 6-8 depict the  $C_L$ ,  $C_D$ , and  $C_M$  values at a range of angles of attack for the experiment and the computed results. All three figures demonstrate improvement of the experimental comparisons with grid refinement. The

drag and moment curves show the largest improvement, whereas the lift curve is only slightly improved with grid refinement. The adapted grid shows the best comparison with experiment for  $C_L$ ,  $C_D$ , and  $C_M$ , and shows evidence of a grid converged solution. It is important to note that all three curves show consistent trends with alpha, matching slopes for  $C_L$  and  $C_M$ , and quantitative matches of  $C_L$ ,  $C_D$  and  $C_M$  within 5% for all angles of attack in the linear regime. Only values of  $C_M$  corresponding to  $C_L$  greater than 0.5 show some deviation from experimental trends. It is important to note that although all solutions were run with numerical parameters consistent with steady-state, there were regions of separated flow observed that could necessitate unsteady time averages be computed, especially at the higher angles of attack.

To ensure that the integrated quantities of lift, drag, and pitching moment comparisons were not fortuitous, quantitative analysis of the surface pressures at various span-wise chord lines were accomplished at an angle of attack of  $0.49^\circ$  where experimentally obtained pressure coefficient data was available.

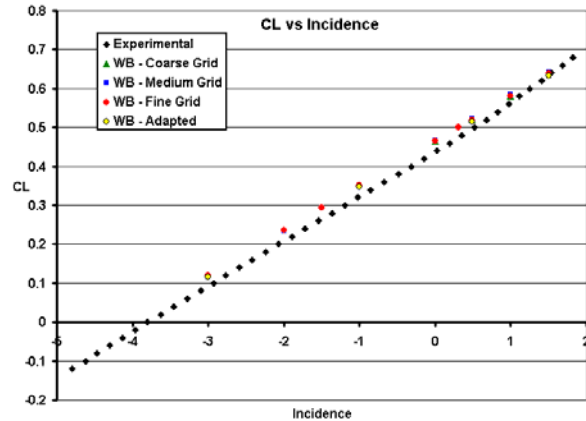


**Figure 6: Plot of  $C_L$  vs Incidence for the wing-body geometry.**

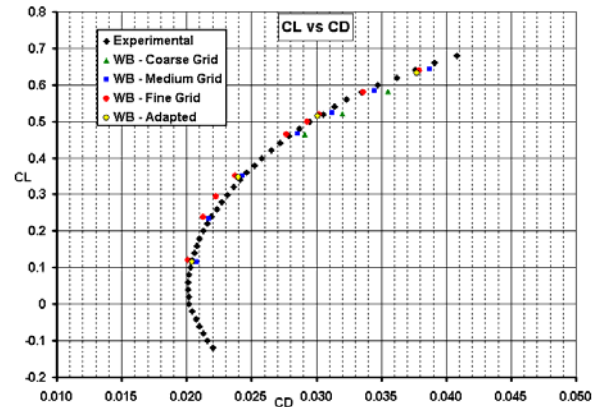


**Figure 7: Plot of  $C_L$  vs  $C_D$  for the wing-body geometry.**

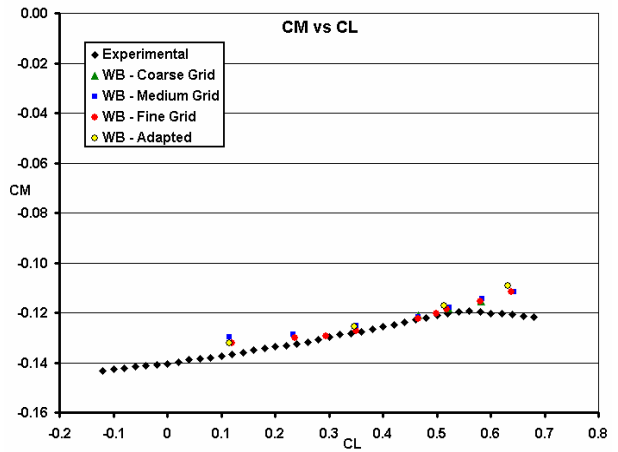


**Figure 8: Plot of  $C_M$  vs  $C_L$  for the wing-body geometry.**

Figures 9-14 depict the  $C_p$  data at various span-wise stations for the  $\alpha = 0.49^\circ$  case. Good agreement between the computations and experiments are observed for all span-wise stations. There appears to be little difference between the three refined grids and the adapted grid. The adapted grid does predict the shock location better and lower  $C_p$  values on the upper wing aft of the shock.

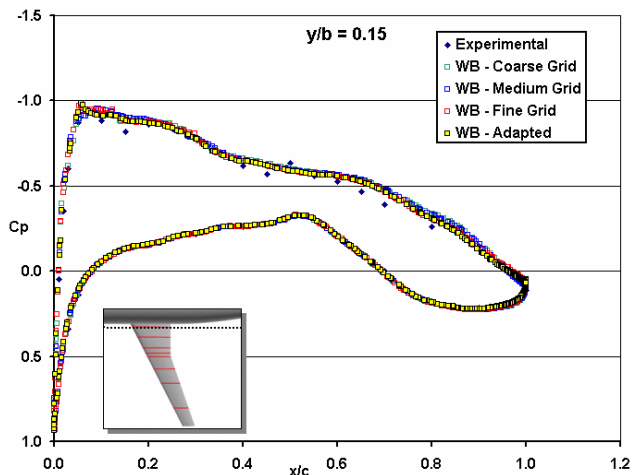


**Figure 9:  $C_p$  plot at  $y/b = 0.15$ ,  $\alpha = 0.49^\circ$ .**

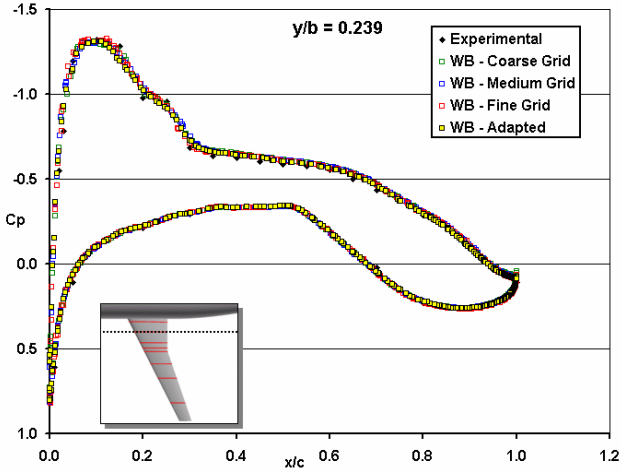


Figure 10: Cp plot at  $y/b = 0.239$ ,  $\alpha = 0.49^\circ$ .

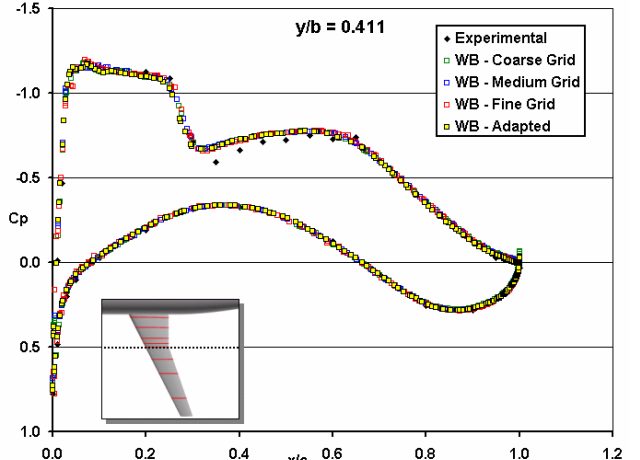


Figure 13: Cp plot at  $y/b = 0.411$ ,  $\alpha = 0.49^\circ$ .

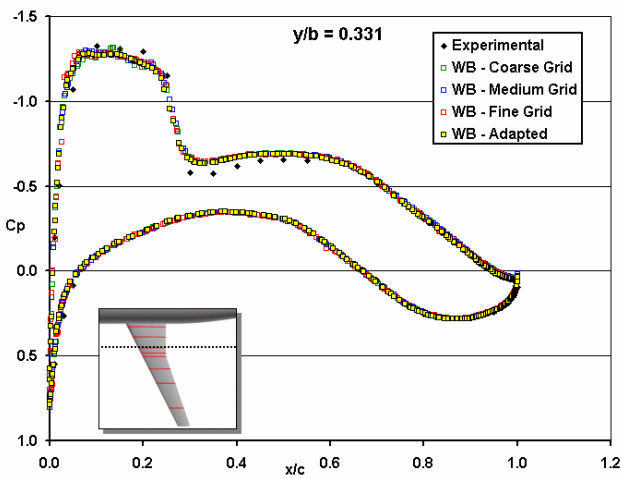


Figure 11: Cp plot at  $y/b = 0.331$ ,  $\alpha = 0.49^\circ$ .

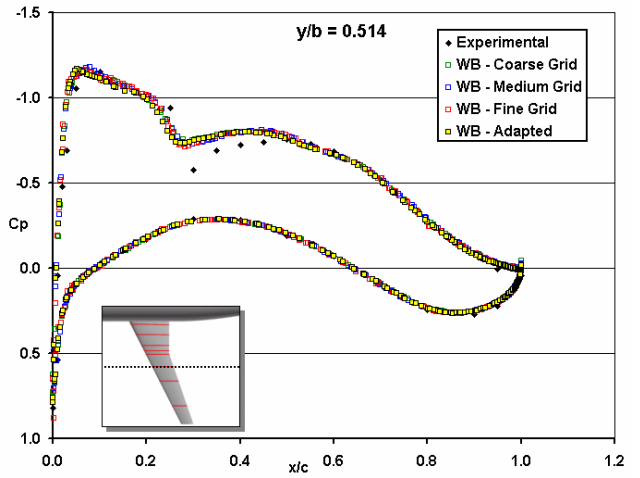


Figure 14: Cp plot at  $y/b = 0.514$ ,  $\alpha = 0.49^\circ$ .

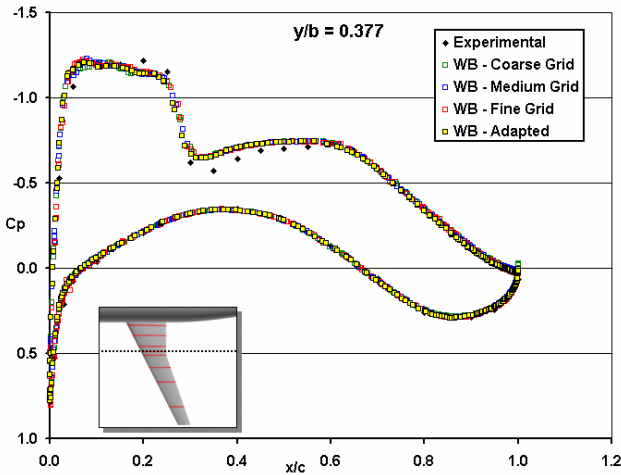
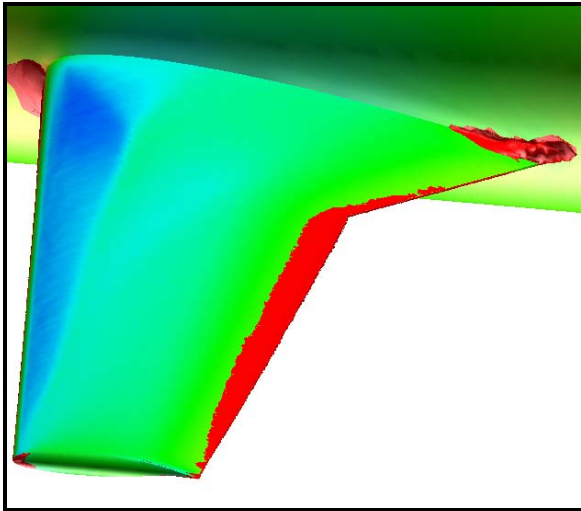
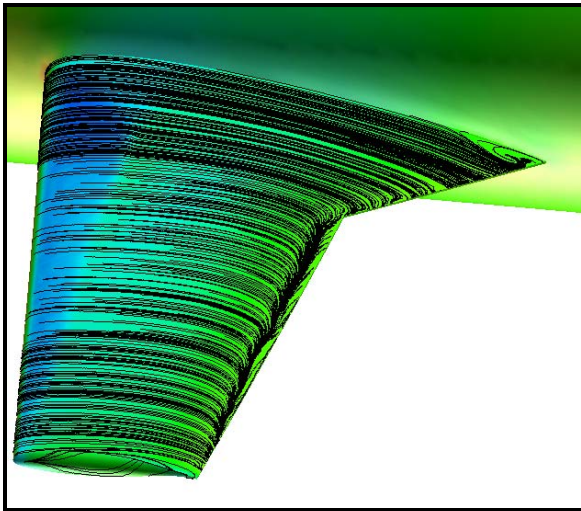


Figure 12: Cp plot at  $y/b = 0.377$ ,  $\alpha = 0.49^\circ$ .

A qualitative view of the flow at  $\alpha = 0.49^\circ$  is shown in Figures 15 and 16. The separated region at the wing root on the upper side, shown in red in Figure 14, was documented in the wind tunnel. However, the narrow separated region along the trailing edge has a much greater impact on integrated forces and moments. This separation is ‘three-dimensional’ since the isosurface calculation factors in all three velocity vectors. The oil flow in Figure 15 confirms the three-dimensionality of the flow at the trailing edge. This separation extends approximately 15% upstream from the trailing edge, impacting the shock location, increasing the pressure drag, and decreasing the skin friction.



**Figure 15:** Separated region show in red. Surface contours of pressure.



**Figure 16:** Oil flow on wing. Surface contours of pressure.

The WBNP single-point convergence data for the fine and adapted grids at  $\alpha = 1.00^\circ$  is presented in Table 6. The experimental alpha for  $C_L = 0.50$  is  $1.00^\circ$  and the computationally predicted alpha is  $0.91^\circ$  following a similar procedure to the WB configuration.

	Experimental	Cobalt	% Diff
$C_L$	<b>0.5005</b>	Fine <b>0.5124</b> Ad <b>0.5140</b>	2.4% 2.7%
$C_D$	<b>0.0338</b>	Fine <b>0.0338</b> Ad <b>0.0338</b>	0% 0%
$C_M$	<b>-0.1199</b>	Fine <b>-0.1147</b> Ad <b>-0.1166</b>	4.3% 2.7%

**Table 6:** Single-point data for the fine and adapted grids at  $\alpha = 1.00^\circ$  for the wing-body-nacelle-pylon case. Computational results are from the fine grid.

The  $C_L$ ,  $C_D$ , and  $C_M$  data at a range of angles of attack for the WBNP configuration are presented in Figures 17-19. The  $CL$ ,  $CD$ , and  $CM$  values compare within 5% for all angles of attack for the WBNP configuration. At the lower angles of attack, the predicted lift slope is less than the experimental lift slope, whereas the two slopes become similar at angles greater than  $0^\circ$ . As is the case with the WB configuration, a comparison of solutions with the experiments improves with grid refinement.

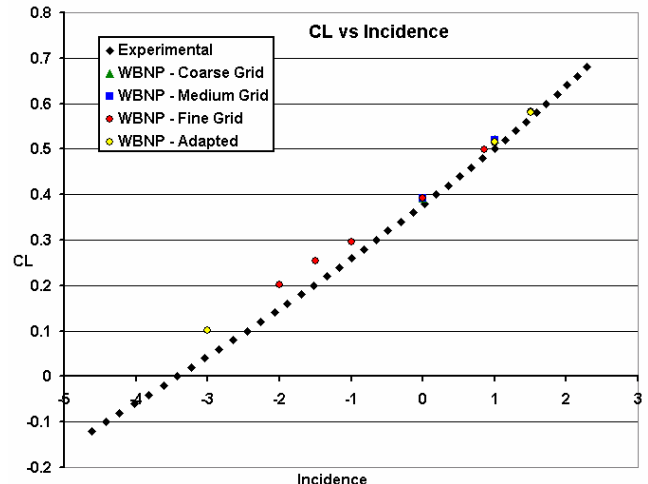


**Figure 17:** Plot of  $C_L$  vs. Incidence for the wing-body-nacelle-pylon geometry.

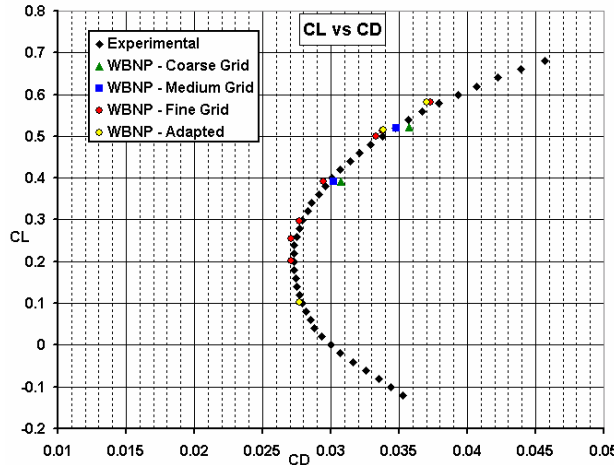


**Figure 18: Plot of  $C_L$  vs.  $C_D$  for the wing-body-nacelle-pylon geometry.**

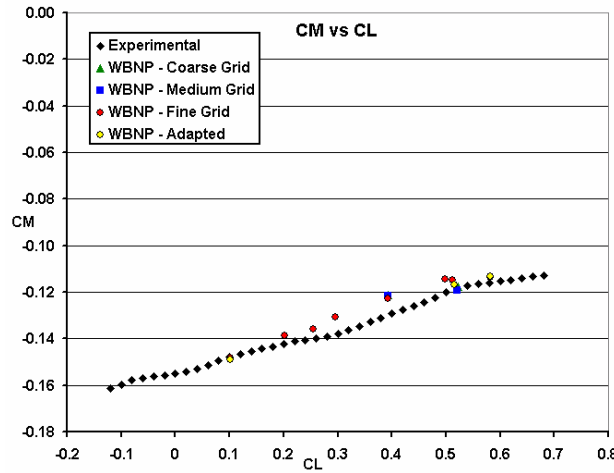


**Figure 19: Plot of  $C_M$  vs.  $C_L$  for the wing-body-nacelle-pylon geometry.**

Figures 20-25 depict the Cp data at various span-wise stations for the alpha = 1.00° case. Good agreement between the computations and experiments are observed for all span-wise stations. Again, there appears to be little difference between the three refined grids and the adapted grid. The adapted grid does predict the shock location better and lower Cp values on the upper wing aft of the shock. The major discrepancy is shown in Figure 22. This station is just inboard of the nacelle and shows the impact of a separation bubble. The refined and the adapted grids produce a larger separation bubble, which is seen in Figure 26 along with the experimental results. The experimentally predicted location is inside of the pressure taps and therefore gives the smooth line in the Cp plot. The fine and adapted grids produce a similar curve that cuts through the bubble. Figure 27 shows the extent of the bubble for the fine and medium grids.

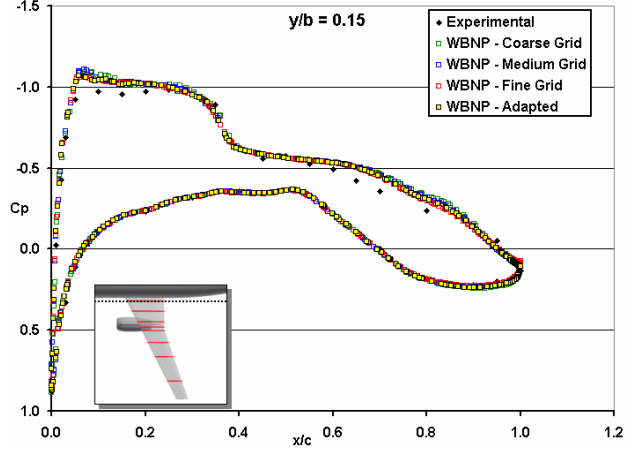


**Figure 20: Cp plot at  $y/b = 0.15$ ,  $\alpha = 1.0^\circ$ .**

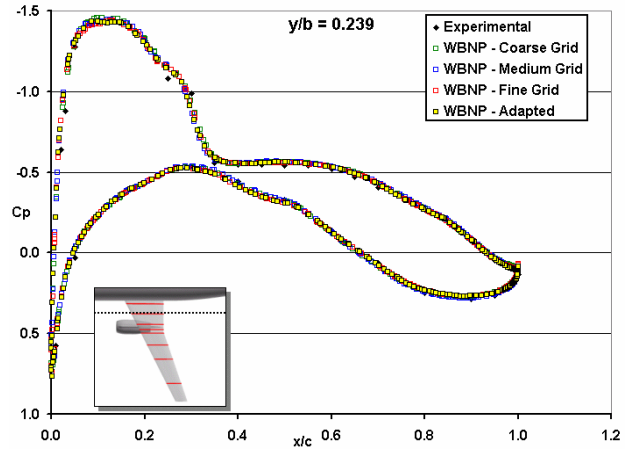


**Figure 21: Cp plot at  $y/b = 0.239$ ,  $\alpha = 1.0^\circ$ .**

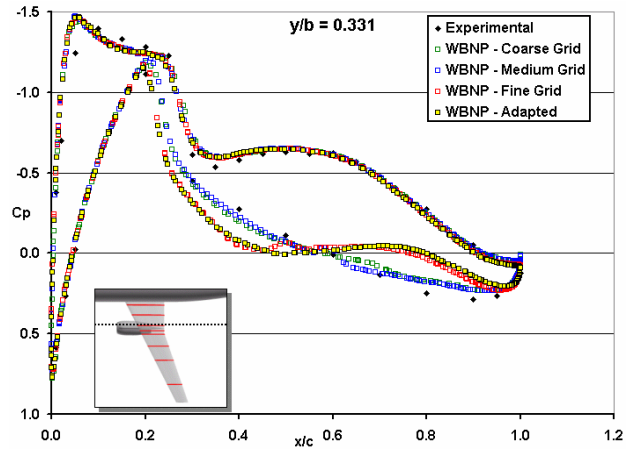


**Figure 22: Cp plot at  $y/b = 0.331$ ,  $\alpha = 1.0^\circ$ .**

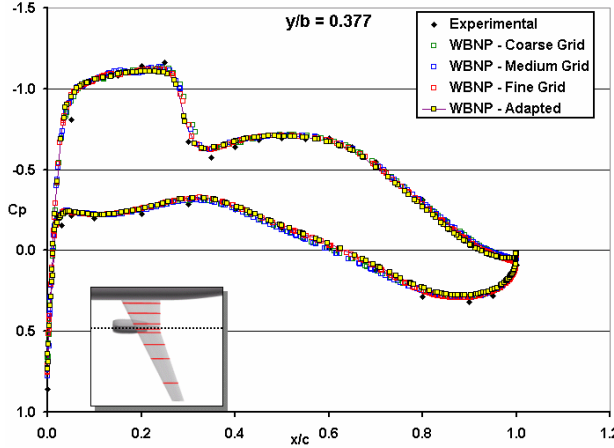


Figure 23: Cp plot at  $y/b = 0.377$ ,  $\alpha = 1.0^\circ$ .

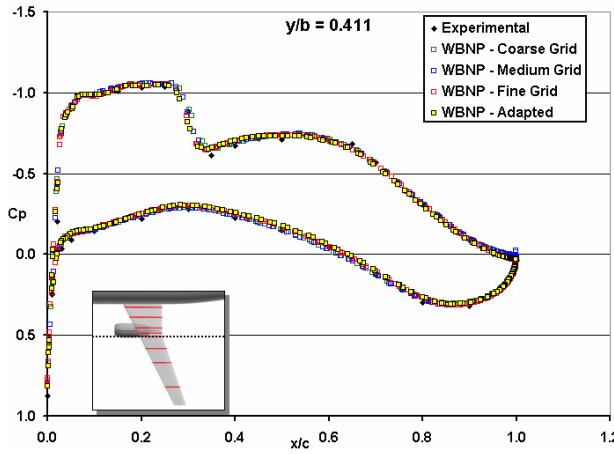


Figure 24: Cp plot at  $y/b = 0.411$ ,  $\alpha = 1.0^\circ$ .

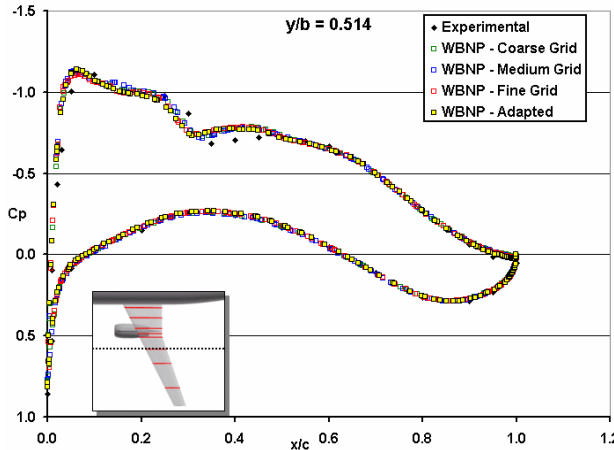


Figure 25: Cp plot at  $y/b = 0.514$ ,  $\alpha = 1.0^\circ$ .

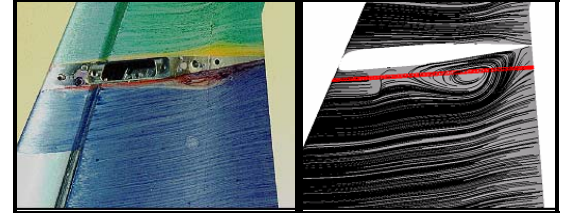


Figure 26: Experimental and fine grid oil flow results. Red line shows pressure taps.

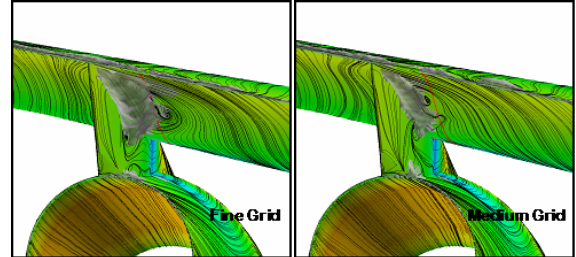


Figure 27: Isosurface of separated flow for the fine and medium grid results. Surface contours of Cp.

A qualitative view of the flow at  $\alpha = 1.00^\circ$  is shown in Figure 28 and 29 similar to the wing-body results. The separated region at the wing root on the upper side, shown in red in Figure 28, was documented in the wind tunnel. However, the narrow separated region along the trailing edge has moved forward on the upper surface when compared to the wing-body flow. This separation impacts the shock location and increases pressure drag and decreases skin friction. There is also a separated region on top of the wing over the nacelle due to shock/boundary layer interaction. The separated region can clearly be seen in the oil flows as well (Figure 29).

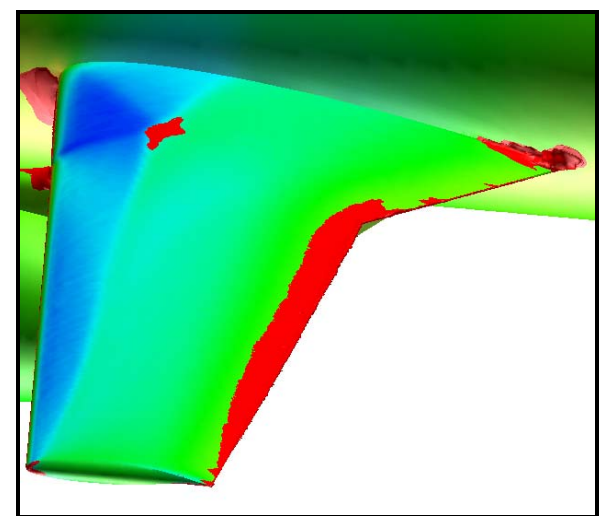
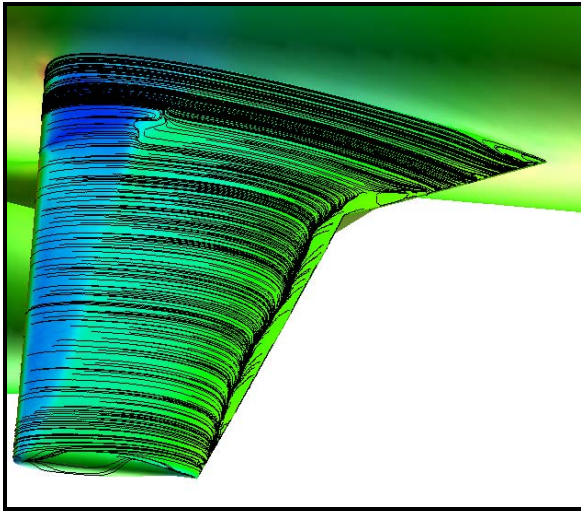


Figure 28: Separated region show in red. Surface contours of pressure.



**Figure 29: Oil flow on wing. Surface contours of pressure.**

A vertical view of the flow topology on the upper surface of the wing is shown in Figure 30. The separated region along the trailing edge is seen on the wind tunnel model, as is the separated region at the wing root and wing kink. Simulations that do not capture these phenomena may have difficulty comparing with the integrated quantities in a consistent manner.



**Figure 30: Experimental and computational oil flow image of upper wing.**

The computationally predicted installation drag for  $CL = 0.500$  for the nacelle/pylon combination is 0.0041 and the experimental installation drag is 0.0043 for a difference of 4.6%. The installation drag comparison for the entire range of angles of attack is shown in Figure 28.

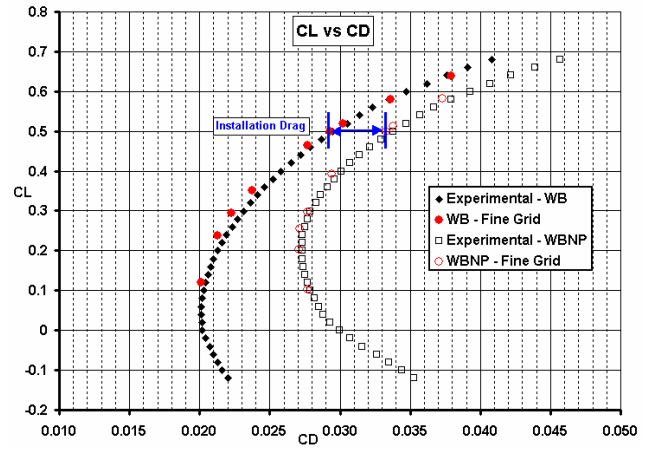


**Figure 31: Installation drag**

### Conclusions

The CFD results computed with *Cobalt* and presented above have shown that increased accuracy in the prediction of forces and moments on an airliner configuration is possible. These simulations can be achieved by using a computational method that allows complete geometry specification with unstructured grids, a low dissipation solver for accurate answers, and state of the art turbulence modeling for actual wind tunnel or flight test condition comparisons. Whereas past uses of CFD have relied on differential calculations to eliminate error sources, current calculations provide absolute comparisons within 5% in CL, CD, and CM allowing industry to use the method in the design cycle. Additionally, a great amount of insight into the flowfield physics can be obtained by using these methods to investigate regions of separation, caused by vortex, shock, and boundary layer interactions.

### References

1. Strang, W. Z., Tomaro, R. F., and Grismer, M. J., "The Defining Methods of Cobalt<sub>60</sub>: A Parallel, Implicit, Unstructured Euler/Navier-Stokes Flow Solver," AIAA Paper 99-0786 Jan. 1999.
2. Tomaro, R.F., Strang, W. Z., and Sankar, L. N., "An Implicit Algorithm for Solving Time Dependent Flows on Unstructured Grids," AIAA Paper 97-0333, Jan. 1997.
3. Grismer, M. J., Strang, W. Z., Tomaro, R. F., and Witzeman, F. C., "Cobalt: A

- Parallel, Implicit, Unstructured Euler/Navier-Stokes Solver," *Advances in Engineering Software*, Vol. 29, No. 3-6, 1998, pp. 365-373.
4. Forsythe, J.R., Strang, W., Hoffmann, K.A., "Validation of Several Reynolds-Averaged Turbulence Models in a 3D Unstructured Grid Code," AIAA Paper 2000-2552, June 2000.
  5. Gottlieb, J. J., and Groth, C. P. T., "Assessment of Riemann Solvers for Unsteady One-Dimensional Inviscid Flows of Perfect Gases," *Journal of Computational Physics*, Vol. 78, 1988, pp. 437-458.
  6. Samareh, J., "Gridtool: A Surface Modeling and Grid Generation Tool," Proceedings of the Workshop on Surface Modeling, Grid Generation, and Related Issues in CFD Solution, NASA CP-3291, May 9-11, 1995.
  7. Pirzadeh, S., "Progress Toward A User-Oriented Unstructured Viscous Grid Generator," AIAA Paper 96-0031, January 1996.
  8. Pirzadeh, S., "Vortical Flow Prediction Using an Adaptive Unstructured Grid Method", Research & Technology Organization Applied Vehicle Technology Panel Meeting, Norway, 7-11 May 2001.